Computational Materials Science 151 (2018) 338–350

Contents lists available at ScienceDirect

Computational Materials Science

journal homepage: www.elsevier.com/locate/commatsci

A numerical approach to compensate for phase field interface effects in alloy solidification

P.C. Bollada*, P.K. Jimack, A.M. Mullis

University of Leeds, United Kingdom

ARTICLE INFO

Keywords:
Crystal formation
Phase field
Alloy solidification
Non-equilibrium thermodynamics
Anti-trapping
Solute trapping

ABSTRACT

The use of a phase field approach to simulate solidification of metallic alloys has many computational advantages, but if obtaining quantitative results relies on the interface between phases being physically realistic, the computational advantage is much reduced. We propose here a method for compensating for a computationally convenient large interface width by simply transferring a numerically derived 1D steady state anti-trapping current to a general non-steady 2D simulation. The method proposed is not restricted to dilute or ideal materials and has a high degree of interface width independence, illustrated here with two models, illustrating a broad applicability for the approach.

1. Introduction

In phase-field modelling of alloy solidification, applying the variational principle to the Gibbs free energy results in equations for phase, solute and temperature, which optimally minimise the Gibbs free energy, see [1]. The principle is clear and elegant but suffers from the practical disadvantage that the length scale of the solid liquid boundary is far smaller than that associated with solute and temperature diffusion. Consequently, phase field modellers of solidification seek to use a larger than physical interface width to make the mathematical system computationally easier to solve. Simple adoption of a larger interface width, though, reveals that solutions are width dependent, see for example [2]. It is generally accepted that the approach to compensate for this is not to be found in a variational formulation, see [3,4] (though, see the discussion in Appendix C which postulates a variational formulation for including anti-trapping currents). Rather, in an approach initiated by [3], one provides an extra degree of freedom at the level of the partial differential equations post variation by typically matching the phase field equations model to a sharp interface model so that the resulting equations have an element of interface width independence. One feature of the application of matched asymptotic analysis to a sharp interface, e.g. [4,5], is that there is necessarily a degree of approximation used in order to simplify the free energy functional to a point where analysis and comparison with sharp interface models becomes tractable. For example, [6] extends [3,4] to use in multiphase models, but only for the simplest thermodynamics. It is of note that models that use physically realistic free energies for complex materials avoid this approach, e.g. [2,7].

The phase field technique for alloy solidification, as established in simpler form by [8] (WBM) is challenged by two phase modelling as described in [9]. This approach associates a unique concentration field, c_L or c_S, for the liquid or solid phases respectively, and the true concentration field is constructed as a weighted average using the phase field. The quantities c_L and c_S are determined through a concentration equation and, crucially, a constraint. The constraint can take the form of proportionality, using a partition coefficient, or by equating the chemical potential. The latter led [10] to unify the methodology using a grand-potential functional (GPF) in place of the usual free energy. This served also to show that the two phase approach was equivalent to a variational formulation, in particular the equal chemical potential constraint in the two-phase formulation is a natural consequence of the new variational technique based on a GPF.

The GPF methodology has been applied in [11] to dilute alloys, but it is notable here that the GPF approach still requires an anti-trapping current to compensate for interface width, and thus, by implication, the model of [9] would benefit from an anti-trapping current to alleviate interface width dependence. [12] argues that the two phase models, with the constant chemical potential across the interface, needs modification for rapid solidification, and suggest modifications that model this: namely, to replace the constant chemical potential constraint with equations for c_L and c_S. It is of note that [12] uses a physically realistic $\delta = 1.875$ nm in their 1D simulations (and so the method advocated in our paper naturally do not apply here). However, for 2D/3D simulations it is likely that larger interface widths will be computationally expedient and thus some method for compensating for artificial solute trapping will become necessary.

* Corresponding author.
E-mail address: p.c.bollada@leeds.ac.uk (P.C. Bollada).

https://doi.org/10.1016/j.commatsci.2018.04.050
Received 13 March 2018; Received in revised form 19 April 2018; Accepted 20 April 2018
Available online 25 May 2018

The GPF approach has also been extended to include non-dilute alloys in [13]. Here, central to the application of GPF is a quadratic approximation of the free energies about the equilibrium concentration values (in a multiphase setting), c_{ij}^E. An approach which does not require approximation to the data bases, for general alloy using an entropy functional is found in [14]. This latter approach is motivated by a general free boundary problem formulation and contains the equal diffusion chemical potentials of the two-phase method as a constraint. For more general thermodynamics the authors state that there is potentially a numerical bottle neck due to this constraint.

We choose to adopt and extend the method of [8] to allow quantitative simulation of more general alloys, without recourse to special cases and approximations. It is of note that the application of the WBM approach to general free energy models has only previously been its extension to multiphase models. Consequently, this work represents a first attempt at quantitative modelling, and modelling in itself, for solidification with arbitrary CALPHAD thermodynamics, whilst allowing a conveniently larger than physical interface width. In this sense the method may be seen as both an extension of [3,8], to allow rapid solidification modelling for arbitrary two phase binary alloys.

A constraint on the phase field approach is that the interface must have sufficient resolution to capture the finest curvature found at the solid-liquid boundary. But typically, tip radii, $\rho \gg d_0 \sim 1$ nm where d_0 is the chemical capillary length, being the same order of magnitude as physical interface width, this being the distance over which long-range atomic ordering is lost at the interface between a crystal and its parent melt and which is typically a few atomic radii. Of more concern is the effect of large interface width on solute partitioning where the maximum and minimum values for solute concentration found at the solid-liquid interface are very much interface width dependent. This effect is known as artificial solute trapping, since it is a model dependent effect that tends to drive the partition coefficient closer to unity. Solute trapping also arises naturally in systems where the velocity of growth is sufficiently high, see [15], which analyses three regimes from low to high growth velocity. We propose here an approach which compensates for artificial (interface width induced) solute trapping, for realistically modelled binary alloys at arbitrary concentration.

In outline, the method we propose consists in solving a 1D steady state problem where the solution not only depends on input values for tip speed and tip interface width (and given tanh profile), but also the strength of an *anti-trapping* current, **j**. We seek the strength of **j** in the steady state 1D problem such that the maximum and minimum values for solute, c, within the interface, coincide with the equilibrium values found from the free energy functions for liquid and solid by well known common tangent construction. Once **j** is found from the 1D problem we apply it to the full (non steady) 2D problem. New values for tip speed and width are extracted from the 2D simulation and used, intermittently, to solve the 1d problem, where the new value for **j** is applied thereon.

We find, for the PbSn alloy tested, and to a large extent model of [8], tested to make connection with a standard model, that this approach gives a high degree of interface independence across a range of measures at the crystal tip. The measures used are tip radius, ρ, tip speed, V, and measures for solute partitioning: $\Delta c \equiv c_L - c_S$ and $k \equiv c_S/c_L$, where c_S is the solid concentration near the tip and c_L is the liquid concentration near the tip.

2. Solute trapping in 1D

In this section we focus on a specific phase-field model for alloy solidification, Pb-Sn in this case, in order to introduce the method proposed to compensate for solute trapping. This is based upon looking at the dependence of solute partitioning on interface width in a steady state 1D scenario.

The phase equations governing the evolution of phase, ϕ, (where $\phi = 0,1$ is solid and liquid respectively) and solute concentration, c, on a domain, Ω, are, respectively (see, for example, [1])

$$\dot{\phi} = -M\frac{\delta F}{\delta \phi}, \tag{1}$$

and

$$\dot{c} = \nabla \cdot D \nabla \frac{\delta F}{\delta c} \tag{2}$$

where

$$F = \int_\Omega f(\phi, \nabla\phi, c)\, \mathrm{d}^3x, \tag{3}$$

M is the mobility and $D = [\phi D_L + (1-\phi)D_S]c(1-c)/(RTv_m)$, with the liquid and solid diffusivities $D_L \gg D_S$, and R and v_m the molar gas constant and the molar volume respectively. The free energy density, f, is decomposed into a surface part, f_S, and bulk part f_B:

$$f = f_S(\phi, \nabla\phi, c) + f_B(\phi, c) \tag{4}$$

where f_B combines, by interpolation, the liquid and solid free energy curves, illustrated in Fig. 1 for a simple constructed example. The surface term is

$$f_S = W(c)\left(\frac{\delta^2}{8}\nabla\phi \cdot \nabla\phi + \phi^2(1-\phi)^2\right) \tag{5}$$

where W is the surface energy of the barrier height between the two phases and δ is a measure of the interface width.

In 1D and at equilibrium Eq. (1) becomes

$$0 = \frac{\delta F_S}{\delta \phi} \tag{6}$$

where

$$F_S = \int_\Omega f_S \, \mathrm{d}x \tag{7}$$

The phase profile,[1]

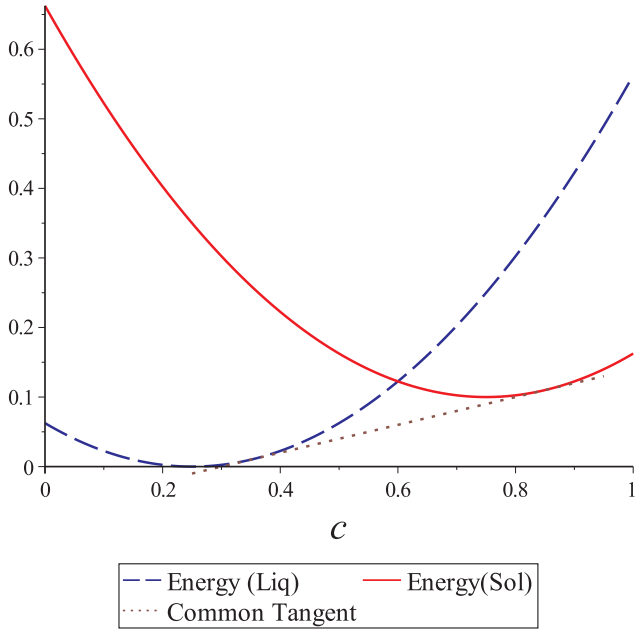

Fig. 1. A constructed example free energy curves, $f^L = (c-0.25)^2, f^S = (c-0.75)^2 + 0.1$ with the common tangent construction that give the equilibrium values of c in the two phases: $c_S^E = 0.85, c_L^E = 0.35$.

[1] more generally the interface width, and even the general shape is modified by the bulk driving term. Some of our tests imply that the resulting profile is well fitted by a continuous piecewise function using two tanh profiles defined on $\phi \in [0,0.5]$ and $\phi \in [0.5,1]$, respectively, though we cannot assert the generality of this result.

$$\phi(x) = \frac{1}{2} + \frac{1}{2}\tanh\left(\frac{2x}{\delta}\right), \tag{8}$$

solves Eq. (6) in 1D, and has the property, $\phi'(x)|_{\phi=1/2} = 1/\delta$ (see appendix A). we adopt the double well potential in Eq. (5), in line with many authors, e.g. [8] in preference to, say, a quadratic potential (a double obstacle) to keep the equations smooth in the bulk: $\phi = 0,1$

The solute equation

$$\dot{c} = \nabla\cdot D\nabla f_c, \tag{9}$$

in 1D becomes

$$\dot{c} = \partial_x D\partial_x f_c, \tag{10}$$

where we use the notation $\partial_x y(x) \equiv \frac{\partial y(x)}{\partial x}$, and the functional derivative $f_c \equiv \frac{\partial f}{\partial c}$. In a comoving coordinate system moving to the right at velocity, u, Eq. (10) becomes

$$0 = \partial_x(D\partial_x f_c + uc). \tag{11}$$

By writing

$$\partial_x f_c = f_{cc}\partial_x c + f_{c\phi}\partial_x\phi \tag{12}$$

one can solve for $c(x)$, once we know $\phi(x)$. We assume, for this purpose, that the 2D phase profile normal to the boundary is well approximated by a tanh function, e.g. Eq. (8), but with a width, δ, ultimately extracted from a 2D simulation. Together with Eq. (12), an initial value for c in the solid, and a value for the tip speed, u, this allows us to solve Eq. (11).

To illustrate the effect of solute trapping we begin with two parabolic example free energy curves for the liquid and solid phases in Fig. 1, where we can extract the equilibrium values for $c_S^E = 0.85$ and $c_L^E = 0.35$ using the common tangent rule.

Using the solid value as a boundary condition, a selection of solutions are given in Fig. 2 for a different values of interface width, δ. Also superimposed in the figure are horizontal lines presenting the equilibrium values for reference, where it is clear that even for the sharpest values chosen for δ, the peaks still do not reach the equilibrium liquid (minimum) value, and for progressively larger δ this minimum increases to get continually closer to the solid (boundary condition) value.

An approach to compensating for the interface width dependency in models with general thermodynamics can be found in [16]. It is based on the observation that including a regularising term in the free energy, $\delta^2\nabla c\cdot\nabla c$, to artificially increase the distance between the two extreme values of c should compensate for the trapping effect. The main problem with this approach is the introduction of 4th order derivatives into the solute equation, which [16] observe can have non-physical effects. On the other hand, a successful adoption of this approach, would result in a variational formulation, with consequent advantages (not least a reliable and thermodynamically consistent formulation of the temperature equation, see [1]).

We adopt a method more in common with the approach pioneered in [3]. To this end, returning to the full dimensional model, the final gradient term in Eq. (9) can be decomposed

$$\nabla f_c = f_{cc}\nabla c + f_{c\phi}\nabla\phi. \tag{13}$$

We will show that compensation for the reduction of partitioning due to the large interface can be achieved by artificially modifying the second term, $f_{c\phi}\nabla\phi$, to give

$$\dot{c} = \nabla\cdot\left(D\nabla\frac{\partial f}{\partial c} + \mathbf{j}\right) \tag{14}$$

where $\mathbf{j} \propto \nabla\phi$. The additional term $\mathbf{j}$ is known as an *anti-trapping current*.

The first appearance of an anti-trapping current is found in [3], which compensates for interface effects in the dilute solution limit (linear solidus and liquidus lines, constant k_E). Using our notation the current is defined by

$$\mathbf{j} = -a\delta\Delta c_0\dot{\phi}\frac{\nabla\phi}{|\nabla\phi|} \tag{15}$$

where $a = 1/(2\sqrt{2})$, and $\Delta c_0 = |c_L^E - c_S^E|$ (where superscript E indicates equilibrium values). The derivation of Eq. (15), along with the determination of relationships between other parameters in the dilute alloy formulation is firmly based on the analysis of sharp interface models for which the phase field formulation is adapted to reproduce. Here, our starting point is the phase field formulation itself and its limiting behaviour as the interface width tends to zero. But rather than investigate this limit we aim to adapt the equations to make them nearly independent of δ in the range $0 < \delta\kappa < 1$ (κ is the tip curvature), where δ is sufficiently small to resolve the curvature but as large as possible otherwise.

We integrate Eq. (11) from a point in the solid where it is assumed the gradients of f_c vanish to give

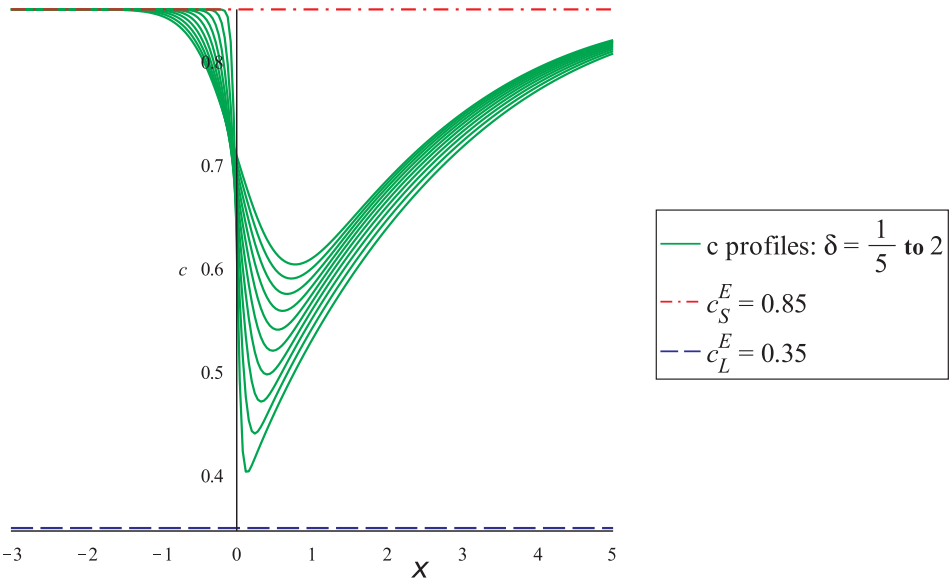

Fig. 2. Example 1D steady state solutions to Eq. (18), for and free energies as in Fig. 1, with various phase field interface widths, $\delta = \frac{1}{5},\frac{2}{5},\ldots,2$. None of the solutions here give the liquid equilibrium minimum, $c_L^E = 0.35$, ($\delta = 1/5$ is the closest, at ~ 0.4).

1D Problem

1. Given a specific u, δ
2. Choose values for $\beta_{\min} = 0$ and $\beta_{\max}$ which bracket β
3. Choose boundary condition $c(x_0) = c_S^E$, where typically $x_0 = -3\delta$.
4. set $\beta = (\beta_{\min} + \beta_{\max})/2$
5. Solve Eq. 24
6. If minimum value of solute, $c_L^m > c_L^E$, set $\beta_{\min} = \beta$ else set $\beta_{\max} = \beta$
7. Repeat steps 4 to 6 until $|c_L^m - c_L^E|$ is less than some tolerance.
8. $\alpha = \beta\lambda$ is the required anti-trapping to apply in the 2D anti-trapping current, Eq. 23.

Fig. 3. Bisection method to find value of the anti-trapping current, β.

$$0 = D\partial_x f_c + u(c - c_S^E) \tag{16}$$

which we rewrite as

$$0 = f_{cc}\partial_x c + f_{c\phi}\partial_x\phi + \frac{u}{D}(c - c_S^E). \tag{17}$$

On inspecting Fig. 2, we can find the local minimum value, c_L^m (or maximum depending on the convention for c), by solving

$$0 = f_{c\phi}\partial_x\phi + \frac{u}{D}(c - c_S^E), \tag{18}$$

with the phase profile

$$\phi = \frac{1}{2} + \frac{1}{2}\tanh\frac{2x}{\delta}. \tag{19}$$

We note that Eq. (19) is only a solution of the equilibrium equation and that the dynamic profile is not a tanh profile, even with different δ. That said, the dynamic profile with a given slope, $1/\tilde{\delta}$ at the interface $\phi = 0.5$ is reasonably well approximated by Eq. (19), but with δ replaced by $\tilde{\delta}$. The method we present uses a given tanh profile, but we take care to extract from the dynamic solution the actual interface width.

We seek to correct c_L^m to make it equal to the equilibrium value, c_L^E by introducing an extra degree of freedom, α, as follows:

$$0 = (1 + \alpha)f_{c\phi}\partial_x\phi + \frac{u}{D}(c - c_S^E). \tag{20}$$

We find, in order to have a minimum, c_L^m, equal to c_L^E, that

$$1 + \alpha = -\frac{u\Delta c_0}{(Df_{c\phi}\partial_x\phi)_{x=x_{\text{liq}}}}, \tag{21}$$

where, recall, $\Delta c_0 \equiv |c_L^E - c_S^E|$, and x_{liq} is the unknown position where the minimum value in the liquid appears (n.b. if we knew x_{liq} we could solve for α directly).

Assuming we have found α, to apply the value of anti-trapping to the non-steady state 2D problem we take the tip velocity to be given by $u = -\dot{\phi}/|\nabla\phi|$ and the $\mathbf{j}$ to be in the direction of the outward normal. Thus, in higher dimensions and non steady state, we write

$$\dot{c} = \nabla\cdot(D\nabla f_c + \mathbf{j}) \tag{22}$$

with

$$\mathbf{j} = \alpha f_{c\phi}\nabla\phi. \tag{23}$$

In practice, we require the anti-trapping to work for a range of values of δ and u, so we search for a value β such that there is a minimum $c = c_L^E$ in the solution of the ode, with $\alpha = \beta\lambda$, i.e.

$$0 = f_{cc}c'(x) + (1 + \beta\lambda)f_{c\phi}\phi'(x) + \frac{u}{D}(c - c_S^E) \tag{24}$$

where λ is the non-dimensional parameter

$$\lambda = \frac{u\delta}{D_L}, \tag{25}$$

with u the tip speed, δ the actual interface width (such that $|\nabla\phi|_{\phi=1/2} = 1/\delta$) and D_L the value of diffusivity in the liquid. This allows us to have $c_L^m \approx c_L^E$ for values from 0 to λ (in particular for speeds $<u$ which will be found away from the tip). We summarize the procedure here in Fig. 3.

We comment on the difference between Eqs. (21) and (24). In Eq. (21) we assume we know where the minimum is located, $x = x_{\text{liq}}$ and so $c'(x_{\text{liq}}) = 0$ by definition. In Eq. (24) we solve and then search for the minimum (or maximum depending on convention) as per the table in Fig. 3. In short, Eq. (21) gives one solution for one u but Eq. (24) gives a range of solutions, which is necessary since u varies around the dendrite.

For our constructed parabolic free energy functions we find a value of $\beta = 4.83$ compensates for interface width dependence in the steady state problem, with diffusivity $D_L = 1, D_S = 0.001, u = 0.2, \delta = 1$. This is illustrated in Fig. 4, where we not only see an exact compensation when $\delta = 1$ but also effective compensation for interface widths, $1/5 < \delta < 2$. Since the interface width only varies slightly around a dendrite, this suggests that, if u,δ are known approximately at the tip, then smaller values of u at other locations on the dendrite surface will benefit from the same value of β (because of Eqs. (24) and (25) the current dependends linearly on u and δ).

In summary, the whole procedure is given in Fig. 5 and, when applied to our constructed example free energy curves, Fig. 1, results in modified solute profiles given in Fig. 4 (to be compared to the no anti-trapping results Fig. 2). The next section looks at the results of applying this procedure to a real complex alloy solution, e.g. Lead-Tin, and the WBM model of Copper Nickel, in single phase growth.

3. Results

This section contains results for a general binary alloy - Lead-Tin and also the simpler Copper-Nickel model of [8]. The anti-trapping method is seen to be effective in both cases, but appears more effective for the more complex model - PbSn.

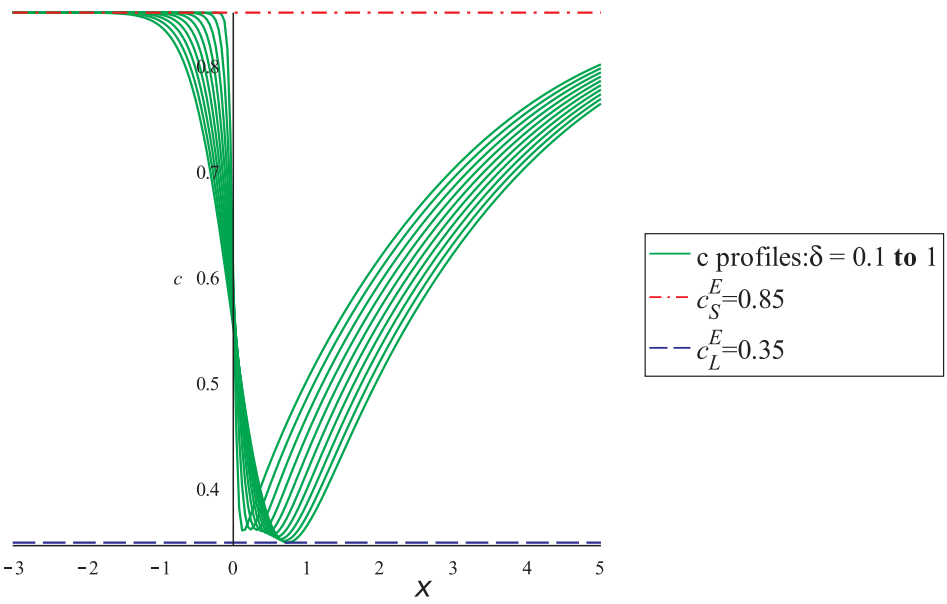

Fig. 4. Solutions to the same steady state 1D problem as illustrated in Fig. 2 but with an anti-trapping current. The value for $\delta = 1$ is chosen to be exact by the choice, $\beta = 4.83$.

1. Make an initial guess for δ, u
2. Set $\phi = 1/2 + 1/2\tanh(2x/\delta)$
3. Find β using Fig. 3
4. Solve the full problem

$$\dot{\phi} = -M\frac{\delta F}{\delta \phi}$$
$$\dot{c} = \nabla \cdot (D\nabla f_c + \mathbf{j}) \tag{26}$$

using the value of β from (3) in

$$\mathbf{j} = -\frac{D}{D_L} f_{c\phi}\beta\delta\dot{\phi}\frac{\nabla\phi}{|\nabla\phi|} \tag{27}$$

where, note, that we have set $\lambda \equiv \delta u/D_L = \delta(-\dot{\phi}/|\nabla\phi|)/D_L$ in $\mathbf{j}$, see Appendix D.

5. Extract values for tip speed, u, and interface width, δ, periodically from the 2D problem and solve the 1D problem to obtain a new value for β.
6. Repeat step 4 and 5. In our implicit code we find every 200 time steps, where our $\Delta t = 1$ns, to be sufficient (and even less often as steady state behaviour is approached), and not time consuming even when dx in the 1D problem is much finer than the 2D simulation.

Fig. 5. The numerical anti-trapping method.

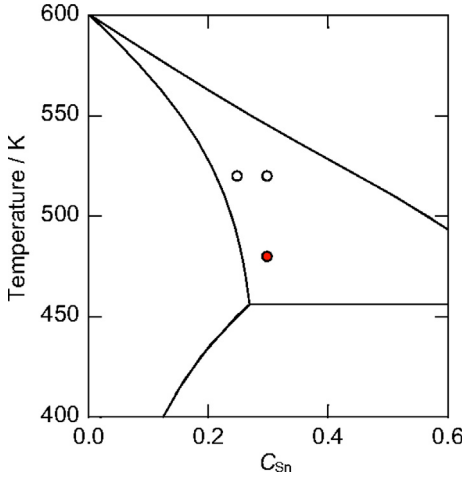

Fig. 6. The phase diagram for Lead-Tin with white circle (520 K and $c_0 = 0.25,0.3$) and red circle (480 K and $c = 0.3$) being the regions of interest explored in the simulations.

3.1. Lead-Tin simulation

In this subsection we explore the effect of anti-trapping with PbSn across different parameters, with and without a thermal field. In particular we explore the single phase growth of the Lead-rich solid phase in the regions indicated in the PbSn phase diagram given in Fig. 6 generated using [17]. We explore the anti-trapping model in both isothermal and thermal conditions. The single thermal run being at 480 K and $c = 0.3$. The complete details of the model and parameters are given in detail in Appendix B where, for example, the units in the plots discussed are detailed in Table 1.

We employ the numerical methods of [18] with a grid size of $\Delta x = 0.39$ and domain size of 800×800 in units of the capillary length d_0.

Table 1
Physical parameters used in the simulation. † these latent heat values are not used in the model which relies on the free energy- see text for detail.

Parameter	Symbol	Value
Char Length	L_0	10^{-9} m
Char speed	V_0	0.2 m s^{-1}
Diffusivity (Liquid)	D_L	10^{-9} m^2 s^{-1}
Diffusivity (Solid)	D_S	10^{-13} m^2 s^{-1}
Capillary length	d_0	10^{-9} m
Initial radius	R_0	$20d_0$
Anisotropy	ϵ	0.02
Surface Energy	σ_A	0.033 J m^{-2}
Surface Energy	σ_B	0.059 J m^{-2}
Melting Temperature (Pb)	T_A	600 K
Melting Temperature (Sn)	T_B	505 K
Operating temperature	T	480,520 K
Initial concenteration	c_0	0.3, 0.25
Mol per unit Vol	ν_m	54730 m^{-3}
Interface width (Pb)	δ_A	$4,8,12 \times d_0$
Interface width (Pb)	δ_B	$\delta_A(T_B/T_A)(\sigma_A/\sigma_B)$
Latent heat	L_A	2.61e8 J m^{-3}†
Latent heat	L_B	9.35e7 J m^{-3}†
Kinetic (Pb)	μ_A	0.0026/m K^{-1} s^{-1}
Kinetic (Sn)	μ_B	0.0031/m K^{-1} s^{-1}
Mobility	M	$(1-c)M_A + cM_B$
Mobility (Pb)	M_A	$\frac{\mu_A T_A}{\sqrt{72} L_A \delta_A}$
Mobility (Sn)	M_B	$\frac{\mu_B T_B}{\sqrt{72} L_B \delta_B}$
Barrier height	W	$= W^A(1-c) + W^B c$
Barrier height (Pb)	W^A	$T_A\sigma_A/(6\sqrt{2}L_A\delta_A)$
Barrier height (Sn)	W^B	$T_B\sigma_B/(6\sqrt{2}L_B\delta_B)$

We inspect the results for the dynamic partition coefficient $k = c_S/c_L$; the normalised partition difference $(c_L - c_S)/\Delta c_0$, where Δc_0 is the difference in equilibrium values; tip radius ρ; and tip speed V. The latter two are in units of $L_0 = 1$ nm and $V_0 = 0.2$ m/s respectively. We plot these quantities against the tip position, and thus these plots reveal the transient values. Steady state quantities may be extracted, in some cases, from the final tip position values if the plot has zero slope. Each sub plot contains three curves for each interface width, both with anti-trapping (AT) and without (NT) (6 plots in total). Broadly, the results without anti-trapping (NT) are interface width dependent and with AT are to a high degree width independent, even in some transient regions. In all the simulations, we find that the AT current has an effect on the actual simulated interface width, i.e. AT tends to reduce δ as compared to that without AT.

In the simulations we control the interface width with an input value δ_e which corresponds to the 1D equilibrium interface width, where the 1D solution is:

$$\phi = 1/2\left[1 + \tanh\left(\frac{2x}{\delta_e}\right)\right]. \tag{28}$$

noting we define the equilibrium interface width

$$\delta_e = \frac{1}{\phi'(x)_{x=1/2}}. \tag{29}$$

Fig. 7 shows results of 6 simulations for three different interface widths (roughly in the range 5 to 10 d_0), with and without anti-trapping. Here the input values (in proportion to the 1D equilibrium interface width) are $\delta_e/\sqrt{8} = 4,6$ and 8 for blue, red and green respectively. These results demonstrate a high degree of interface width independence when AT is used, and, conversely, a δ dependence without AT. The two smaller interface widths display convergence for all quantities measured, but the highest δ disagrees slightly in the tip radius.

Fig. 8 shows the equivalent set of results but with a change to the initial condition, $c_0 = 0.25$, effectively making this a larger undercooling. In this case the input values are also $\delta_e/\sqrt{8} = 4,6$ and 8 for blue, red and green respectively. Here the discrepancy between the AT results and the non-AT results is more marked, but still the agreement amongst the AT results is again very close: in particular there is agreement even in the tip radius for all widths.

Fig. 9 shows the equivalent set of results but with a change to the initial condition, $c_0 = 0.3, T = 480$ K. For stability, the input values are reduced to $\delta_e/\sqrt{8} = 3,4$ and 6 for blue, red and green respectively. Here the discrepancy between the AT results and the non-AT results becomes greater still, nevertheless the agreement within the AT results is very close. Even the largest interface width $\delta = 6.78$ approaches the steady state value of tip radius, ρ.

The thermal-solute phase field model, we employ, is detailed in Appendix B. This results in results given in, Fig. 10, we adjust the 1D solve to depend on tip velocity, V, the interface width at the tip, δ, and the temperature at the tip, T_i. The far field temperature, T_0, was set at 480 K and the tip temperature, T_i was found to rise to 503.7 K. At T_i, the equilibrium values from the common tangent values for c are of course different to those associated with T_0, and are the natural choice for the 1D solve, i.e. we use T_i not T_0 to extract the AT current.

3.2. Simulations using WBM model

In order to explore the wider applicability of our technique towards interface width independence, and also to make connection with a simpler and well known model, we give results of simulations using the benchmark model found in [8]. This model, known as WBM, in fact, forms the basis for our model for PbSn, and by extension, any model using data base free energies in this way.

We use the model and parameters as described in [8, Table 1] with

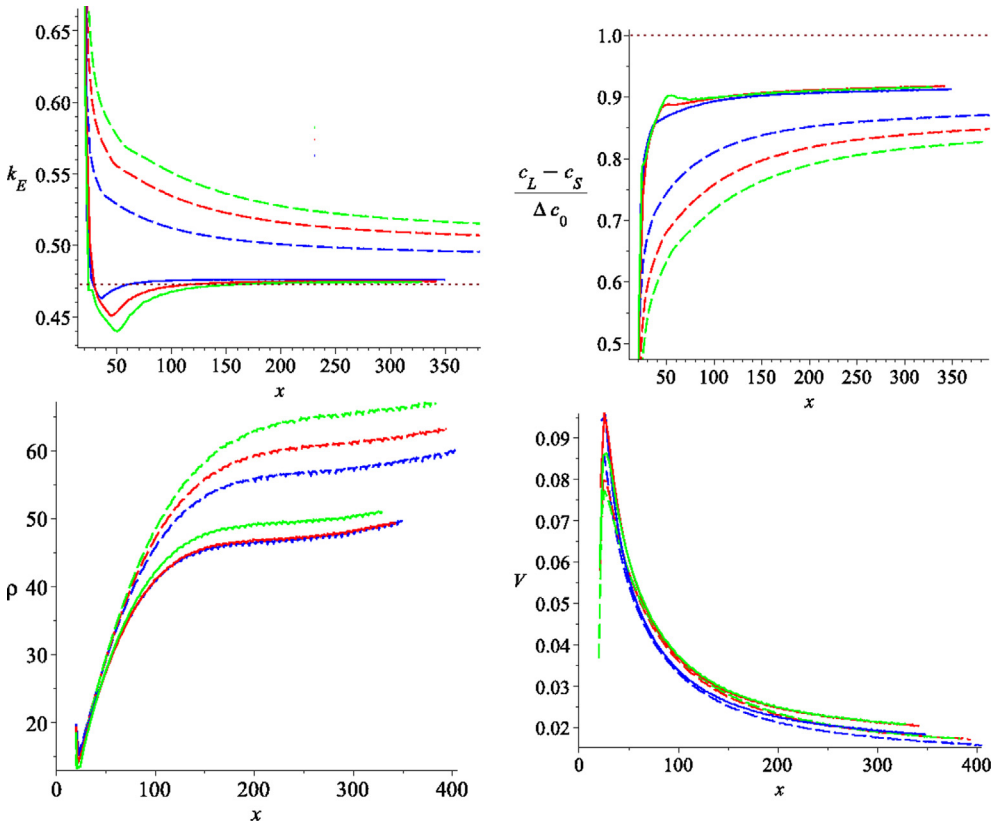

Fig. 7. Results for PbSn, $c_0 = 0.3$,$T = 520$ K, $\delta_e/\sqrt{8} = 4,6,8$ (blue, red and green respectively). Clockwise from top left: dynamic partition coefficient, k_E; concentration difference normalised with equilibrium value $\Delta c/\Delta c_0$; tip speed,V; tip radius, ρ. The dashed results are without the anti-trapping and solid lines with anti-trapping. There is a high degree of interface independence for the latter across all measures. All dimensioned quantities are in units of length, $L_0 = 1$ nm and velocity, $V_0 = 0.2$ m/s as given in Table 1. (For interpretation of the references to colour in this figure legend, the reader is referred to the web version of this article.)

the exception of the kinetic parameters, $[\mu_{\mathrm{Ni}},\mu_{\mathrm{Cu}}] = [2.00,2.47]\,\mathrm{mK}^{-1}\,\mathrm{s}^{-1}$, which we found computationally difficult and so have reduced these by a factor of 100 to $\mu = [0.02,0.0247]$. One feature of the model given in [8] is that the equilibrium concentrations depend on the interface width, δ (via their expression for free energy Eqs. (8) to (10) and the expression for barrier height Eq. 36 in [8]). Hence, we chose a particular reference δ so that the equilibrium concentrations as given by [8] are $c_S = 0.16$ and . This is in contrast to most other users of the model who restrict the model's application to either dilute alloys, or where partitioning is negligible, e.g. [19].

Application of our method to WBM results in Fig. 11, which illustrates Δc at all points around an early dendrite (where $\Delta c = c_L - c_S$ can be given as a function of angle, $\theta \in [0,\pi/2]$, between a point on the 2D dendrite's surface to the x-axis - see Fig. 12 for the corresponding dendrite shapes). In the figure the dotted line indicates Δc_0, the equilibrium value. It is clear that there is convergence of Δc across a small range of input parameters, $\delta_e/\sqrt{8} = 4,6,8$. The simulation was on a domain of 800×800 with $\Delta x = 0.39$ and so there are between 10 to 20 grid points across the interface.

The main feature of Fig. 11 is the convergence, not just at the tip ($\theta = 0,\pi/2$), but also to a high degree throughout the surface. The anti trapping current is computed from the tip speed and by design, a low speed reduces the current. Thus we expect good convergence at the tip and in between the dendrite arms (where the speed is much reduced). The agreement in between these extremes is due to a reasonable assumption that the amount of anti-trapping is in linear proportion to speed. On the other hand there is not convergence when there is no anti-trapping- "NT". The dashed curves in Fig. 11 make perfect sense in terms of the known deficiencies of the model. Growth is slowest at $\pi/4$ so interface induced trapping is lowest and the solution is closest to equilibrium. Conversely, for $\theta = 0,\pi/2$ velocity is at a maximum, so the largest departure from equilibrium is to be expected.

A plot of all the corresponding dendrites is given in Fig. 12, all at the same tip position. Clearly there is better agreement with the anti-trapping model between the different interface values, which may be contrasted with the straight phase field model (dashed lines). The figure adds weight to the assertion that even qualitatively, dendrite formation may well be incorrect without anti-trapping.

4. Discussion

The immediate observation from the above results is that compensating for solute trapping alone seems good enough to give results with a high degree of interface independence. Clearly, as is commonly accepted and is the case here, the interface width must still be less that the tip radius. The rule of thumb being $\delta < \rho/2$. Yet the 1D solve uses equilibrium values for c_S^E and c_L^E which differ significantly from the values found in the dynamic setting, as should be expected since there is natural solute trapping for higher velocities associated with increasing undercooling. The question that needs to be addressed is: why does the use of equilibrium values from the 1D steady state model give such satisfactory results in the dynamic setting where the dynamic partition

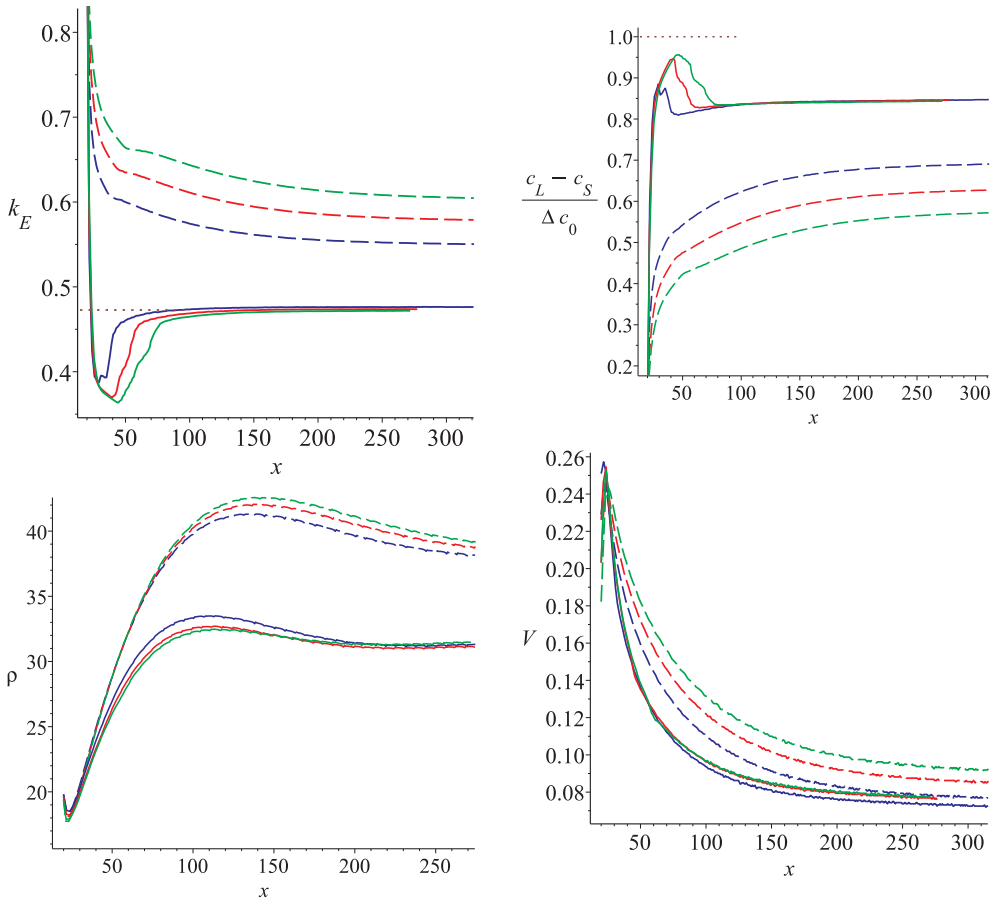

Fig. 8. Results for PbSn, $c_0 = 0.25$,$T = 520$ K, $\delta_e/\sqrt{8} = 4,6,8$ (blue, red and green), Clockwise from top left: dynamic partition coefficient, k_E; concentration difference normalised with equilibrium value $\Delta c/\Delta c_0$; tip speed,V; tip radius, ρ. The dashed results are without the anti-trapping and solid lines with anti-trapping. There is a high degree of interface independence for the latter across all measures. All dimensioned quantities are in units of length, $L_0 = 1$ nm and velocity, $V_0 = 0.2$ m/s as given in Table 1. (For interpretation of the references to colour in this figure legend, the reader is referred to the web version of this article.)

values, c_S and c_L are (significantly) different from the equilibrium ones? An intuitive answer to this can be made by examining the case where the far field (and initial condition) for c_0 is increased to a point where the undercooling is reduced to near equilibrium and the tip velocity becomes very small. In this scenario, the equilibrium values for c_S^E and c_L^E are unchanged and are approached by the dynamic values, and the only change for the 1D solve is the lower tip speed. The results above suggest that there is a near linear proportionality between tip speed, V, and the size of anti trapping in all the cases considered above. The Peclet number for these simulations is, $Pe = \rho V/D_L \sim 0.5$. The prediction, therefore, is that the method might be less effective in situations with significantly higher Peclet numbers.

For small V, [8] propose a model for the partition coefficient, in their notation

$$k = k_E(1 - VM^{-1}\Gamma_0) \tag{30}$$

where, in our model, we write this with $\widetilde{V} \equiv 2V\tau_0/(3d_0)$

$$k = k_E[1 - \overline{V} + O(\widetilde{V}^2)] \tag{31}$$

where $\tau_0 = 1/MW$ and the capillary length $d_0 \sim (2/3)/\Gamma_0 \equiv (2/3)/\int_{-\infty}^{\infty}(\phi_x)^2 dx$ for an interface width $\delta \sim d_0$. Now, since the chosen characteristic time and lengths in our simulations are τ_0 and d_0, we can read off the non-dimensional number, $\widetilde{V} \equiv (2/3)V\tau_0/d_0$ from the figures, the highest being from Fig. 9, where $\widetilde{V} \approx 0.153 \times (2/3) \sim 0.102$. Thus indicating $k \sim 0.898k_E$. Our result in Fig. 9, for the value for the smallest $\delta = 4d_0$ being: $k/k_E = 0.887$, which is clearly very close to this linear prediction.

Finally, in Appendix C we seek to put the anti-trapping current into a thermodynamic context. This not only shows that the anti-trapping term can be put into a variational form, but also that the anti-trapping current is approximately entropy neutral. We then go on to make a connection with other work, [22], which postulates a cross term, related to anti-trapping, in the phase field equation.

5. Conclusion

We have presented a scheme to compensate for interface width dependence in general phase field modelling of metallic alloys. The scheme consists of a steady state 1D solve to extract an anti-trapping current, **j**, such that equilibrium partition values for solute are retained independent of the interface width. This value for **j** is then applied, to a general 2D simulation, with the modification that the anti-trapping is proportional to velocity and interface width (which vary along the dendrite surface). This straightforward approach is seen to be very effective in the first unsteady problem chosen, across a range of temperatures and solute concentration, and also in the WBM benchmark problem.

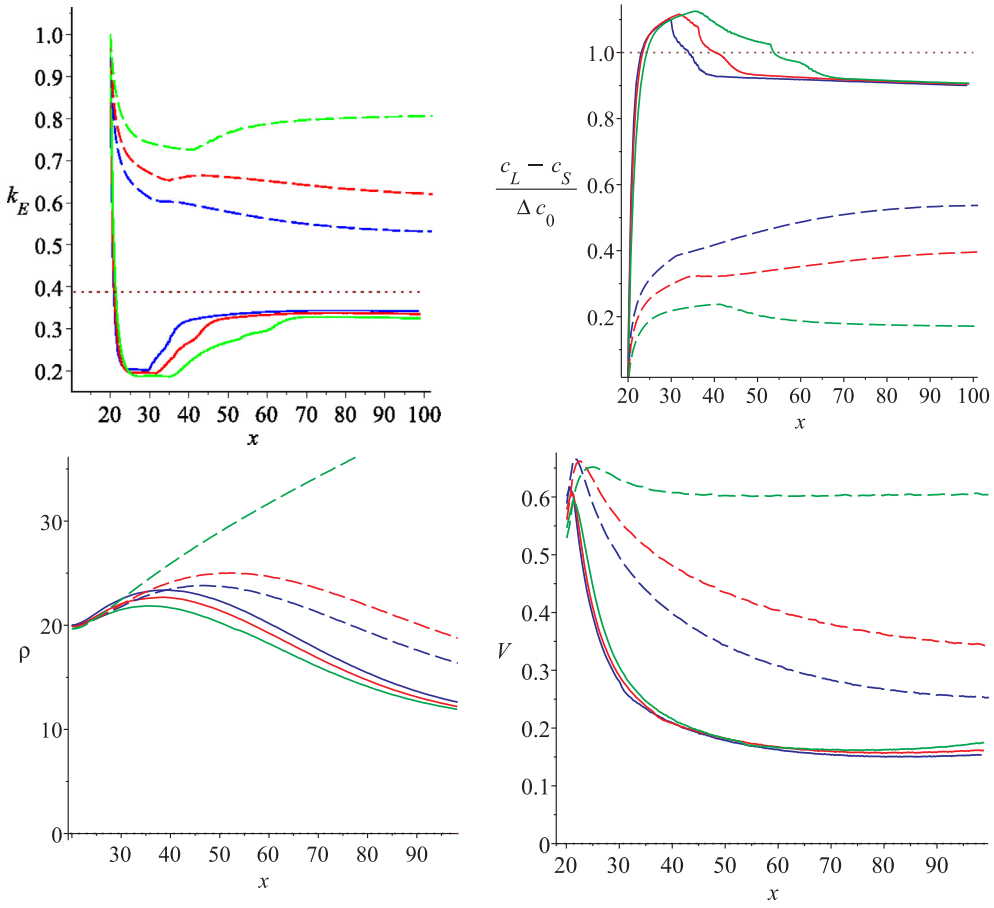

Fig. 9. Results for PbSn at the highest undercooling, $c_0 = 0.3, T = 480$ K, $\delta_e/\sqrt{8} = 3,4,6$ (blue, red green). Clockwise from top left: dynamic partition coefficient, k_E; concentration difference normalised with equilibrium value $\Delta c/\Delta c_0$; tip speed, V; tip radius, ρ. The dashed results are without the anti-trapping and solid lines with anti-trapping. There is a high degree of interface independence with AT for the latter across all measures, but without, the results disagrees significantly for different $\delta_e/\sqrt{8}$ (and so δ). All dimensioned quantities are in units of length, $L_0 = 1$ nm and velocity, $V_0 = 0.2$ m/s as given in Table 1. (For interpretation of the references to colour in this figure legend, the reader is referred to the web version of this article.)

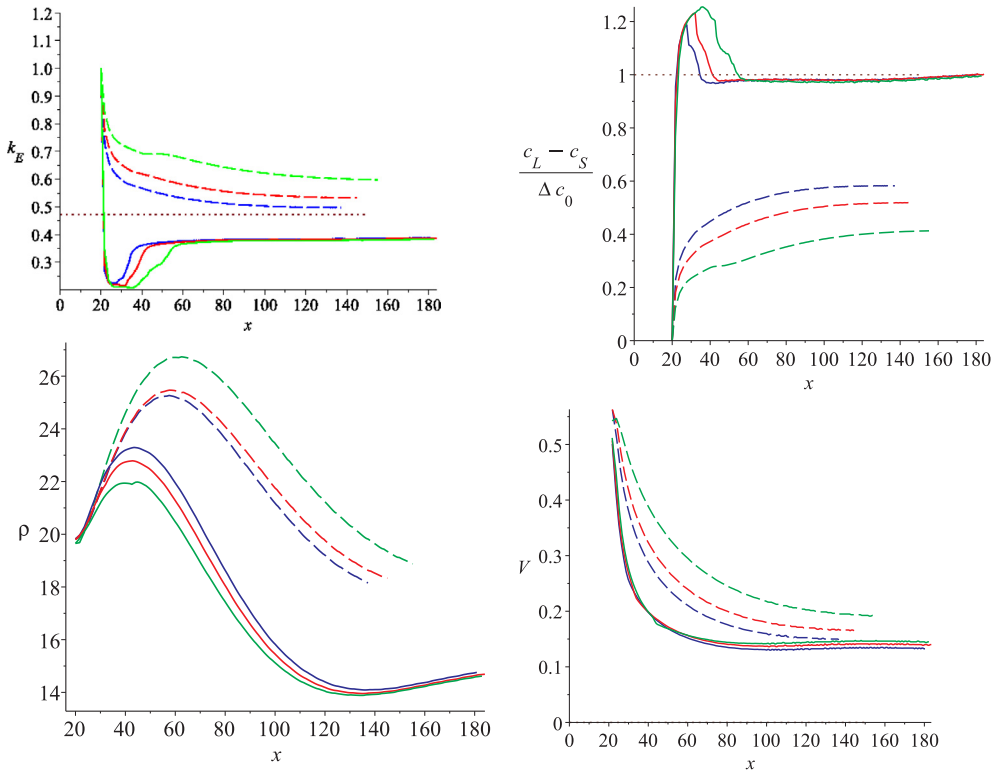

Fig. 10. Results for PbSn at the highest undercooling, $c_0 = 0.3$,$T = 480$ K, with a thermal field. Clockwise from top left: dynamic partition coefficient, k_E; concentration difference normalised with equilibrium value $\Delta c/\Delta c_0$; tip speed,V; tip radius, ρ. The dashed results are without the anti-trapping and solid lines with anti-trapping. There is a high degree of interface independence with AT for the latter across all measures, but without, the results diverge significantly for different δ_e. All dimensioned quantities are in units of length, $L_0 = 1$ nm and velocity, $V_0 = 0.2$ m/s as given in Table 1.

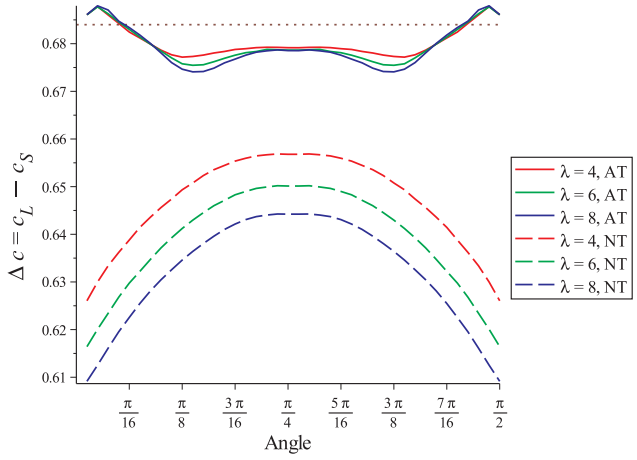

Fig. 11. Plot of Δc against the angle subtended between the x-axis and a point on the dendrite surface. The dotted line represents equilibrium Δc_0. The lowest velocity is found at $\pi/4$ and the highest being at the tip - $\theta = 0,\pi/2$. The effect of interface width on Δc is much more noticeable without anti-trapping for all $\theta \in [0,\pi/2]$.

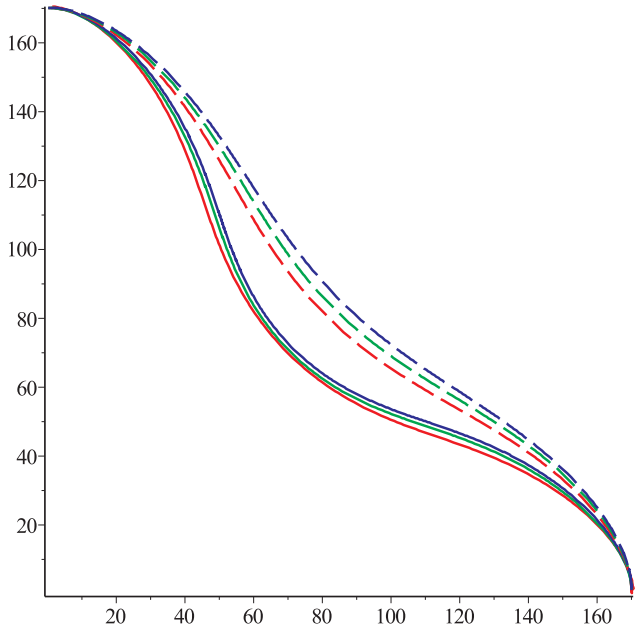

Fig. 12. A plot of the corresponding dendrites (using the same color code as Fig. 11). We see that there is broad agreement between the profiles associated with the anti-trapping. Without anti-trapping one can see that the trend with larger interface widths is towards a rounded diamond shape normally associated with near equilibrium growth (Wulff shape).

Acknowledgements

This research was funded by EPSRC Innovative Manufacturing Research Hub in Liquid Metal Engineering (LiME), Grant No. EP/N007638/1.

Appendix A. Equilibrium 1D solution to the phase field equations

Beginning with the 1D equilibrium functional equation, Eq. (6),

$$\frac{\delta F_S}{\delta \phi} = \int_\Omega \left[\frac{\delta^2}{8} \nabla\phi \cdot \nabla\phi + \phi^2 (1-\phi)^2 \right] \mathrm{d}x = 0 \tag{32}$$

is follows, by applying the variation derivative, that

$$\frac{\delta^2}{8} \nabla^2 \phi = 2\phi(\phi-1)(2\phi-1) \tag{33}$$

which, upon substitution, is satisfied by Eq. (8) as required.

Appendix B. Model detail and parameters

One of the simulations had a dynamic temperature field for which we used the model detailed in [1]

$$C_p \dot{T} = \nabla \cdot \kappa \nabla T - \left(1 - T\frac{\partial}{\partial T}\right)\frac{\partial f}{\partial \phi}\dot{\phi} \tag{34}$$

where $C_p \equiv -T\frac{\partial^2 f}{\partial T^2}, \kappa = 100 D_L$. The other parameters and functions used in the PbSn model are given below in the tables:

In Table 1, indicated by †, the latent heat values are evaluated using $E(\phi,c,T) \equiv -(1-T\frac{\partial}{\partial T})\frac{\delta F}{\delta \phi}$ with $L_A = \Delta E|_{\mathrm{Pb}} \equiv E(1,0,T_A) - E(0,0,T_A)$ and $L_B = \Delta E|_{\mathrm{Sn}} \equiv E(1,1,T_B) - E(0,1,T_B)$, where $\phi = 1(0)$ is liquid(solid), and $c = 0(1)$ is Pb(Sn).

The bulk free energy is given by interpolating between solid and liquid free energies using the monotonic function, $g = \phi^2(3-2\phi)$, to give

$$\begin{aligned}
f_B &= g(\phi) f^L(c,T) + g(1-\phi) f^S(c,T) + S_M(c,T),\\
S_M &= RT[c\ln c + (1-c)\ln((1-c)],\\
f^L &= (1-c) g_A^L(T) + c g_B^L(T) + f_{RK}^L(c,T),\\
f^S &= (1-c) g_A^S(T) + c g_B^S(T) + f_{RK}^S(c,T),\\
g_A^L &= \sum_{i=1}^{8} h_A^{L,i} T_i(T), \quad g_B^L = \sum_{i=1}^{8} h_B^{L,i} T_i(T),\\
g_A^S &= \sum_{i=1}^{8} h_A^{S,i} T_i(T), \quad g_B^S = \sum_{i=1}^{8} h_B^{S,i} T_i(T),\\
f_{RK}^L &= \sum_{i=1}^{2} (f_1^{L,i} + T f_2^{L,i}) c_i(c), \quad f_{RK}^S = \sum_{i=1}^{2} (f_1^{S,i} + T f_2^{S,i}) c_i(c).
\end{aligned} \tag{35}$$

These functions are the standard way CALPHAD methodology, [20], represents solute-thermal dependence. Here f_{RK} indicates Redlich-Kister model; S_M indicates the entropy of mixing; and the pure thermal dependence is given by Gibbs vector constants and functions in the following array:

i	$h_A^{L,i}$	$h_B^{L,i}$	$h_A^{S,i}$	$h_B^{S,i}$	$T_i(T)$
1	−2977.961	1247.957	−7650.085	−345.135	1
2	93.949561	51.355548	101.700244	56.983315	T
3	−24.5242231	−15.961	−24.5242231	−15.961	$T\ln(T)$
4	−0.365895e−2	−0.188702e−1	−0.365895e−2	−0.188702e−1	T^2
5	−0.24395e−6	0.3121167e−5	−0.24395e−6	, 0.3121167e−5	T^3
6	0.00	−61960.0	0.00	−61960.0	$1/T$
7	−0.6019e−18	0.147031e−17	0.00	0.00	T^7
8	0.00	0.00	0.00	0.00	$1/T^9$

The Redlich-Kister contants and functions are given by:

i	$f_1^{L,i}$	$f_2^{L,i}$	$f_1^{S,i}$	$f_2^{S,i}$	$c_i(c)$
1	6204.5	−.67981	7145.3	−2.30237	$c(1-c)$
2	791.7	−1.5219	0	0	$c(1-c)(1-2c)$

(36)

Appendix C. A variational form for anti-trapping

In this section we wish to postulate how the addition of the anti-trapping current, **j**, may be formulated within a variational framework. One application of this is to inspect the contribution of **j** to entropy production, and since changes in interface width have negligible effect on entropy production it follows that there is a requirement on **j** to be entropy neutral.

It is explained in [1] that the binary alloy formulation, Eqs. (1) and (2), used in this paper can be derived from

$$\dot{A} = [A,F] \tag{37}$$

where, A is an arbitrary functional and the bracket is defined

$$[A,F] = -\int_\Omega M\frac{\delta A}{\delta\phi}\frac{\delta F}{\delta\phi}\,\mathrm{d}^3x - \int_\Omega D\nabla\frac{\delta A}{\delta c}\cdot\nabla\frac{\delta F}{\delta c}\,\mathrm{d}^3x. \tag{38}$$

To produce a solute equation with a current, see Eq. (14), we can postulate an additional term to the bracket of

$$-\int_\Omega \mathbf{j}\cdot\nabla\frac{\delta A}{\delta c}\,\mathrm{d}^3x \tag{39}$$

which produces the extra term, $\nabla\cdot\mathbf{j}$ in:

$$\dot{c} = \nabla\cdot D\nabla f_c + \nabla\cdot\mathbf{j}, \tag{40}$$

by design. Now, by noting that $\mathbf{j} \propto \dot{\phi}\mathbf{n} \propto \frac{\delta F}{\delta\phi}\mathbf{n}$ we can rewrite the bracket term Eq. (39) as

$$-\int_\Omega \Lambda\frac{\delta F}{\delta\phi}\mathbf{n}\cdot\nabla\frac{\delta A}{\delta c}\,\mathrm{d}^3x \tag{41}$$

where $\Lambda\frac{\delta F}{\delta\phi}\mathbf{n} = \mathbf{j}$ includes all the parameters such as, M,D,α etc. The full bracket is now

$$[A,F] = -\int_\Omega M\frac{\delta A}{\delta\phi}\frac{\delta F}{\delta\phi}\,\mathrm{d}^3x - \int_\Omega D\nabla\frac{\delta A}{\delta c}\cdot\nabla\frac{\delta F}{\delta c}\,\mathrm{d}^3x - \int_\Omega \Lambda\frac{\delta F}{\delta\phi}\mathbf{n}\cdot\nabla\frac{\delta A}{\delta c}\,\mathrm{d}^3x. \tag{42}$$

Which gives the anti-trapping model in bracket form and therefore implies that the anti-trapping model can be derived from a variational form. Following the methods of [1] we can see there is entropy production $\dot{s}_{AT}$,due to this term of

$$\dot{s}_{AT} = \frac{\Lambda}{T}\frac{\delta F}{\delta\phi}\mathbf{n}\nabla\frac{\delta F}{\delta c} \equiv \frac{1}{T}\mathbf{j}\cdot\nabla f_c \tag{43}$$

If we make the assumption, by the common tangent rule (and the non-equilibrium extension of that rule given in [8]), that f_c is equal either side of the interface (i.e. $f_c^S \equiv f_c|_{\phi=0} = f_c|_{\phi=1} \equiv f_c^L$), and $\mathbf{j}$ is approximately constant, we find by integrating across the interface that

$$\dot{S} \equiv \int_L^S \dot{s}_{AT}\,\mathrm{d}x = \frac{1}{T}|\mathbf{j}|(f_c^S - f_c^L) \approx 0. \tag{44}$$

The significance of this result is that the anti-trapping term is entropy neutral, and thus, for example, need not be included in the temperature equation and does not contribute to free energy minimisation. This single observation explains why the anti-trapping current not only corrects solute partitioning but also, to a large extent, creates interface width independence across a range of measures.

Finally it is possible to postulate a symmetric form of anti-trapping by writing

$$\begin{aligned}[A,F] = &-\int_\Omega M\tfrac{\delta A}{\delta\phi}\tfrac{\delta F}{\delta\phi}\,\mathrm{d}^3x - \int_\Omega D\nabla\tfrac{\delta A}{\delta c}\cdot\nabla\tfrac{\delta F}{\delta c}\,\mathrm{d}^3x\\ &\int_\Omega \Lambda\tfrac{\delta F}{\delta\phi}\mathbf{n}\cdot\nabla\tfrac{\delta A}{\delta c}\,\mathrm{d}^3x + \int_\Omega \Lambda\tfrac{\delta A}{\delta\phi}\mathbf{n}\cdot\nabla\tfrac{\delta F}{\delta c}\,\mathrm{d}^3x.\end{aligned} \tag{45}$$

which gives the following phase field formulation

$$\dot{\phi} = -M\frac{\delta F}{\delta\phi} + \Lambda\mathbf{n}\cdot\nabla f_c, \tag{46}$$

and

$$\dot{c} = \nabla\cdot D\nabla f_c - \nabla\cdot\Lambda\frac{\delta F}{\delta\phi}\mathbf{n}. \tag{47}$$

This formulation above is very similar to as mentioned in [22], being a development on their previous work [21]. The difference is that in our formulation, $\mathbf{j} \propto \mathbf{n}\frac{\delta F}{\delta\phi}$, but in [22] $\mathbf{j} \propto \mathbf{n}\dot{\phi}$. Exploration of the above is beyond the scope of this paper and is left for future work.

Appendix D. Relating the 1D anti-trapping current to 2D/3D

Starting with the 1D equation, Eq. (24),

$$0 = f_{cc}c'(x) + (1+\beta\lambda)f_{c\phi}\phi'(x) + \frac{u}{D}(c - c_S^E) \tag{48}$$

multiply by D and differentiate with respect to x gives

$$0 = \partial_x[D(f_{cc}c'(x) + f_{c\phi}\phi'(x) + \beta\lambda f_{c\phi}\phi'(x))] + uc'(x) \tag{49}$$

Setting $uc'(x) = -\dot{c}$ gives

$$\dot{c} = \partial_x[D(f_{cc}c'(x) + f_{c\phi}\phi'(x) + \beta\lambda f_{c\phi}\phi'(x)] \tag{50}$$

and so converting to 2D/3D gives

$$\dot{c} = \nabla\cdot[D(f_{cc}\nabla c + f_{c\phi}\nabla\phi + \beta\lambda f_{c\phi}\nabla\phi)] = \nabla\cdot[D(\nabla f_c + \beta\lambda f_{c\phi}\nabla\phi)] = \nabla\cdot(D\nabla f_c + D\beta\lambda f_{c\phi}\nabla\phi)$$

Thus $\mathbf{j} = D\beta\lambda f_{c\phi}\nabla\phi = -\frac{D}{D_L}\delta f_{c\phi}\dot{\phi}\frac{\nabla\phi}{|\nabla\phi|}$.

References

[1] P.C. Bollada, P.K. Jimack, A.M. Mullis, Bracket formalism applied to phase field models of alloy solidification, Comp. Mat. Sci 126 (2017) 426–437.
[2] C.W. Lan, Y.C. Chang, C.J. Shih, Adaptive phase field simulation of non-isothermal free dendritic growth of a binary alloy, Acta Mater. 51 (2003) 1857–1869.
[3] A. Karma, Phase-field formulation for quantitative modeling of alloy solidification, Phys. Rev Lett. 87–11 (2001) 115701.
[4] B. Echebarria, Quantitative phase-field model of alloy solidification, Phys. Rev. E 70 (2004) 061604.
[5] N. Opoku, A quantitative multi-phase field model of polycrystalline alloy solidification, Acta Mater. 58 (6) (2010) 2155–2164.
[6] R. Folch, M. Plapp, Quantitative phase-field modeling of two-phase growth, Phys. Rev. E 72 (2005) 011602.
[7] J. Eiken, Multiphase-field approach for multicomponent alloys with extrapolation scheme for numerical application, Phys. Rev. E 73 (2006) 066122.
[8] A.A. Wheeler, W.J. Boettinger, G.B. McFadden, Phase-field model for isothermal phase transitions in binary alloys, Phys. Rev. A 45 (10) (1992) 7424–7440.
[9] S.G. Kim, W.T. Kim, T. Suzuki, Phase-filed model for binary alloys, Phys. Rev E 60 (6) (1999) 7186–7197.
[10] M. Plapp, Unified derivation of phase-field models for alloy solidification from a grand-potential functional, Phys. Rev. E 84 (2011) 31601.
[11] A. Choudhury, B. Nestler, Grand-potential formulation for multicomponent phase transformations combined with thin-interface asymptotics of the double-obstacle potential, Phys. Rev. E 85 (2012) 21602.
[12] I. Steinbach, L. Zhang, M. Plapp, Phase-field model with finite interface dissipation, Acta Mater. (2012) 2689–2701.
[13] A. Choudhury, M. Kellner, B. Nestler, A method for coupling the phase-field model on a grand-potential formalism to thermodynamic databases, Curr. Opin. Solid State Mater. Sci. 287–300 (2015) 19.
[14] M. Ohno, T. Takaki, Y. Shibuta, Variational formulation of a quantitative phase-field model for nonisothermal solidification in a multicomponent alloy, Phy. Rev. E 33311 (2017) 96.
[15] K. Glasner, Solute trapping and the non-equilibrium phase diagram for solidification of binary alloys, Physica D 151 (2001) 253–270.
[16] A.A. Wheeler, W.J. Boettinger, G.B. McFadden, Phase-field model of solute trapping during solidification, Phys. Rev. E 47 (3) (1993) 1893–1909.
[17] J. Groebner, H.L. Lukas, F. Aldinger, CALPHAD 20 (1996) 2247–2254.
[18] P.C. Bollada, C.E. Goodyer, P.K. Jimack, A.M. Mullis, F.W. Yang, Three dimensional thermal-solute phase field simulation of binary alloy solidification, J. Comput. Phys. 287 (2015) 130–150.
[19] M. Conti, Growth of a needle crystal from an undercooled alloy melt, Phys. Rev. E 56 (3) (1997) 3197–3202.
[20] H. Ohtani, K. Okuda, K. Ishida, Thermodynamic study of phase equilibria in the Pb-Sn-Sb system, J. Phase Equil. 16 (5) (1995) 416–429.
[21] E.A. Brener, G. Boussinot, Kinetic cross coupling between nonconserved and conserved fields in phase field models, Phys. Rev. E 86 (2012) 060601.
[22] G. Boussinot, E.A. Brener, Interface kinetics in phase-field models: Isothermal transformations in binary alloys and step dynamics in molecular-beam epitaxy, Phys. Rev. E 88 (2013) 022406.